Commun. Comput. Phys.
doi: 10.4208/cicp.280711.230312a

Vol. **13**, No. 4, pp. 1107-1133
April 2013

Development of an Explicit Symplectic Scheme that Optimizes the Dispersion-Relation Equation of the Maxwell's Equations

Tony W. H. Sheu[1,2,3,*], L. Y. Liang[1] and J. H. Li[1]

[1] *Department of Engineering Science and Ocean Engineering, National Taiwan University, No. 1, Sec. 4, Roosevelt Road, Taipei, Taiwan.*
[2] *Taida Institute of Mathematical Science (TIMS), National Taiwan University, Taiwan.*
[3] *Center for Quantum Science and Engineering (CQSE), National Taiwan University, Taiwan.*

Received 28 July 2011; Accepted (in revised version) 23 March 2012

Available online 21 September 2012

Abstract. In this paper an explicit finite-difference time-domain scheme for solving the Maxwell's equations in non-staggered grids is presented. The proposed scheme for solving the Faraday's and Ampère's equations in a theoretical manner is aimed to preserve discrete zero-divergence for the electric and magnetic fields. The inherent local conservation laws in Maxwell's equations are also preserved discretely all the time using the explicit second-order accurate symplectic partitioned Runge-Kutta scheme. The remaining spatial derivative terms in the semi-discretized Faraday's and Ampère's equations are then discretized to provide an accurate mathematical dispersion relation equation that governs the numerical angular frequency and the wavenumbers in two space dimensions. To achieve the goal of getting the best dispersive characteristics, we propose a fourth-order accurate space centered scheme which minimizes the difference between the exact and numerical dispersion relation equations. Through the computational exercises, the proposed dual-preserving solver is computationally demonstrated to be efficient for use to predict the long-term accurate Maxwell's solutions.

AMS subject classifications: 52B10, 65D18, 68U05, 68U07

Key words: Maxwell's equations, non-staggered grids, zero-divergence, fourth-order, dual-preserving solver, dispersion relation equations.

1 Introduction

In Maxwell's equations, two field variables $\underline{B}$ (magnetic flux density) and $\underline{D}$ (electric flux density) are theoretically constrained by the solenoidal conditions given by $\nabla\cdot\underline{B}=0$ and

*Corresponding author. *Email address:* twhsheu@ntu.edu.tw (T. W. H. Sheu)

$\nabla \cdot \underline{D} = 0$. Provided that these two zero-divergence constraint equations are imposed initially, the field variables $\underline{B}$ and $\underline{D}$ governed by the coupled Faraday's and Ampère's equations can remain divergence free within the continuous context. In many numerical calculations of Maxwell's equations, the divergence-free conditions for the magnetism and electricity are unfortunately not satisfied due to some inevitably introduced discretization errors. The inability to retain the zero-divergence constraint conditions (or the Gauss's law) may result in a numerical instability problem when simulating the electromagnetic wave propagation. How to resolve this non-divergence problem becomes one of the major research themes in the development of a proper Maxwell's equation solver [1]. One can enforce these divergence-free constraint conditions all the time in the well known Yee's staggered grids [2]. The generalized Lagrange multiplier formulation of Munz et al. [3] belongs to the other class of numerical methods that can be applied to retain also the divergence-free condition in the Maxwell's equations. One can get a local divergence-free Maxwell's solution as well using the discontinuous Galerkin finite element method introduced in [4].

When approximating the derivative terms, dissipation error can smear the solution and at the same time dispersion error can cause an erroneously predicted phase speed or group velocity. Since Maxwell's equations contain only the first-order spatial derivative terms, the indispensable dispersion error can more or less destabilize the scheme. It is therefore essential to reduce the dispersion error when approximating the first-order spatial derivative terms. How to get an accurately predicted propagation characteristics during the simulation of Maxwell's equations becomes the second objective of the present study.

Discretization error is always cumulative. After solving the electromagnetic wave equations for a long time, the computed time-evolving solution will be gradually deteriorated by the non-symplectic temporal schemes. Failure to preserve the symplectic geometric structure can very often lead to numerical instability problem after a long time simulation. How to preserve symplecticity embedded in the Maxwell's equations for a long-term computation poses another difficulty, thus motivating us to properly approximate the time derivative terms shown in the Faraday's and Ampère's equations.

The rest of this paper will be organized as follows. In Section 2, the Maxwell's equations, which include the Faraday's law for the time-evolving magnetic flux density, Ampère's law for the propagation of electric flux density, and the Gauss' laws for ensuring the solenoidal nature of the magnetism and electricity, will be presented. In Section 3 two divergence-free constraints are imposed on the electric and magnetic vector fields. In Section 4, the first-order spatial derivative terms in the coupled Faraday's and Ampère's equations will be approximated in a way that the computed difference between the exact and numerical dispersion relation equations is minimized. Since Maxwell's equations are classified to be Hamiltonian (Eq. (2.8)), we will apply a symplectic structure-preserving time integrator to conserve its symplecticity numerically using the explicit symplectic partitioned Runge-Kutta scheme. We will also present in the same section a detailed analysis of the scheme in Fourier space. In Section 5, one problem with the exact solution

will be chosen to validate the proposed second-order temporally accurate scheme and fourth-order spatially accurate scheme. Finally, we will draw some conclusions based on the solutions computed in non-staggered grids.

2 Working equations

The following set of vector equations will be solved in time domain to get the magnetic field intensity $\underline{H}$ and the electric field density $\underline{E}$:

$$\frac{\partial \underline{H}}{\partial t} = -\frac{1}{\mu} \nabla \times \underline{E}, \tag{2.1}$$

$$\frac{\partial \underline{E}}{\partial t} = \frac{1}{\epsilon} \nabla \times \underline{H}. \tag{2.2}$$

Two constitutive relations for relating the electric and magnetic fluxes to the electric and magnetic fields are required to make the system of differential equations fully determined. The permeability μ in the Faraday's law of induction and the permittivity ϵ in the Ampère's law are assumed to be homogeneous and isotropic. In the non-absorbing region, these material parameters are the proportional constants shown in the linear isotropic constitutive relations $\underline{D} = \epsilon\, \underline{E}$ and $\underline{B} = \mu\, \underline{H}$, where $\underline{B}$ and $\underline{D}$ are denoted as the magnetic induction (or magnetic flux density) and the electric displacement (or electric flux density), respectively. Note that the wave propagation speed c $(\equiv(\varepsilon\,\mu)^{-1/2})$ depends on the magnitudes of ϵ (dielectric permittivity) and μ (magnetic permeability).

Eqs. (2.1)-(2.2) will be solved in a domain without considering the current density and charge. The transport equations for $\underline{H}$ and $\underline{E}$ in (2.1)-(2.2) are constrained by the following two equations, which constitute the Gauss' laws, for the respective magnetism and electricity

$$\nabla \cdot \underline{B} = 0, \tag{2.3}$$

$$\nabla \cdot \underline{D} = 0. \tag{2.4}$$

Eqs. (2.3)-(2.4) are satisfied automatically if they are divergence-free initially [4]. The entire set of equations (2.1)-(2.4), as a result, is a mathematically over-determined system in the sense that one can neglect Eqs. (2.3)-(2.4) in the differential context. We will resolve this issue in Section 3.

By defining $\underline{X}(t) = \mu^{\frac{1}{2}} \underline{H}(t)$ and $\underline{Y}(t) = \epsilon^{\frac{1}{2}} \underline{E}(t)$, the time-evolving equations (2.1)-(2.2) can be expressed in terms of these variables as

$$\frac{\partial}{\partial t}(\underline{X}, \underline{Y}(t))^T = \underline{\underline{M}}_{2\times 2}(\underline{X}(t), \underline{Y}(t))^T. \tag{2.5}$$

The two-by-two matrix $\underline{\underline{M}}$ contains the differential operator and has the components given by

$$M_{11} = M_{22} = 0, \qquad M_{12} = -\frac{1}{\mu^{\frac{1}{2}}} \nabla \times \frac{1}{\epsilon^{\frac{1}{2}}}, \qquad M_{21} = \frac{1}{\epsilon^{\frac{1}{2}}} \nabla \times \frac{1}{\mu^{\frac{1}{2}}}. \tag{2.6}$$

Let $\underline{\psi}(t)=(\underline{X}(t),\underline{Y}(t))^T$, the time-dependent set of Maxwell's equations is read as

$$\frac{\partial \underline{\psi}(t)}{\partial t}=\underline{\underline{M}}\,\underline{\psi}(t). \tag{2.7}$$

The resulting formal solution can be easily derived as $\underline{\psi}(t)=\exp(t\underline{\underline{M}})\,\underline{\psi}(t=0)$ [6]. Owing to the time evolving operator $\exp(t\underline{\underline{M}})$, the solution of the electromagnetic wave will evolve in an exponential sense.

Maxwell's equations cast in the curl form can be transformed to the following set of equivalent vector equations for the solution vector $\underline{z}=(Hx,Hy,Hz,Ex,Ey,Ez)^T$

$$\underline{\underline{\mathrm{N}}}\,\underline{z}_t+\sum_{k=1}^{3}\underline{\underline{\mathrm{K}}}_k\,\underline{z}_k=\nabla_z S(\underline{z}). \tag{2.8}$$

The skew symmetric matrix $\underline{\underline{\mathrm{N}}}$ and the three symplectic structures $\underline{\underline{\mathrm{K}}}_k$ $(k=1-3)$ have been detailed in [7]. Because of the existence of Eq. (2.8), Maxwell's equations are classified to be a set of mutltisymplectic Hamiltonian partial differential equations (HPDEs). Provided that the Hamiltonian function for the energy functional $S(\underline{z})$ is independent of $\underline{x}$ and t, Maxwell's equations can be expressed differently by the following mathematically equivalent local energy conservation law form

$$\frac{\partial\, P(\underline{z})}{\partial t}+\sum_{k=1}^{3}\frac{\partial\, Q_{\underline{\mathrm{k}}}(\underline{z})}{\partial X_k}=0, \tag{2.9}$$

where [7]

$$P(\underline{z})=S(\underline{z})-\frac{1}{2}\sum_{k=1}^{3}\underline{z}^T\underline{\underline{\mathrm{K}}}_k\underline{z}_k,\qquad Q_k(\underline{z})=\frac{1}{2}\underline{z}^T\underline{\underline{\mathrm{K}}}_k\underline{z}. \tag{2.10}$$

Along the solution vector $\underline{z}$, Maxwell's equations accommodate the following multisymplectic conservation law (MSCL)

$$\frac{\partial\omega}{\partial t}+\sum_{k=1}^{3}K_k=0, \tag{2.11}$$

where $\omega\equiv d\underline{z}\wedge\underline{\underline{\mathrm{N}}}d\underline{z}$ and $K_k\equiv d\underline{z}\wedge K_k\,d\underline{z}$ $(k=1-3)$ [7]. By virtue of the local energy conservation law (or Eq. (2.8)), the total energy conservation law for the Maxwell's equations can be derived as follows

$$\int_\Omega\left(\frac{1}{\epsilon}\,\underline{H}\cdot\nabla\times\underline{H}+\frac{1}{\mu}\,\underline{E}\cdot\nabla\times\underline{E}\right)d\Omega=\int_\Omega\left(\underline{H}\cdot\frac{\partial E}{\partial t}-\underline{E}\cdot\frac{\partial H}{\partial t}\right)d\Omega. \tag{2.12}$$

In other words, Eqs. (2.1)-(2.4) have the following Hamiltonian functional H [8]

$$H(\underline{H},\underline{E})=\frac{1}{2}\int_\Omega\left(\frac{1}{\epsilon}\,\underline{H}\cdot\nabla\times\underline{H}+\frac{1}{\mu}\,\underline{E}\cdot\nabla\times\underline{E}\right)d\Omega. \tag{2.13}$$

It is also worthy to point out here that Eqs. (2.1)-(2.2) conserve the following two invariants

$$W_1(t)=\int_\Omega (\epsilon\ \underline{E}\cdot\underline{E}+\mu\ \underline{H}\cdot\underline{H})\ d\Omega, \tag{2.14}$$

$$W_2(t)=\int_\Omega \left(\epsilon\left|\frac{\partial \underline{E}}{\partial t}\right|^2+\mu\left|\frac{\partial \underline{H}}{\partial t}\right|^2\right) d\Omega. \tag{2.15}$$

Note that $W_1(t)$ is defined as the energy density.

3 Divergence-free-preserving solution algorithm

Maxwell's equations in (2.1)-(2.4) contain three Faraday's equations for $\underline{B}$, three Ampère's equations for $\underline{D}$, and two Gauss' equations for the respective magnetism and electricity. In this system of eight differential equations, two of them need to be abandoned for uniquely getting the solutions for the total number of six unknowns. Eqs. (2.3) and (2.4) are normally left out of consideration since the Gauss law for $\underline{H}$ and $\underline{E}$ is valid as a direct consequence of the Faraday's law and Ampère's law, respectively, in the continuous context.

Discretization error for the Faraday's and Ampère's equations may make the magnetic and electric field equations no longer solenoidal. Blackbill and Barnes [9] pointed out that the nonzero terms $\nabla\cdot\underline{H}$ and $\nabla\cdot\underline{E}$ appear as the forces parallel to the field. The problem regarding the discretely predicted nonzero $\nabla\cdot\underline{H}$ and $\nabla\cdot\underline{E}$ must be eliminated. Otherwise, it is impossible to get the Maxwell's solutions that satisfy Eqs. (2.3)-(2.4) all the time.

One way of resolving the computational difficulty regarding the omission of Gauss's law in the course of calculating Maxwell's equations is to introduce a penalty term to force the magnetic and electric divergences towards zero [10–12]. Employment of this idea calls for an addition of two gradient terms for the scalar variables Φ_1 and Φ_2 to Eqs. (2.1) and (2.2), respectively. The resulting modified Faraday's and Ampère's equations turn out to be

$$\frac{\partial \underline{E}}{\partial t}-\frac{1}{\epsilon}\nabla\times\underline{H}+\nabla\Phi_1=0, \tag{3.1}$$

$$\frac{\partial \underline{H}}{\partial t}+\frac{1}{\mu}\nabla\times\underline{E}+\nabla\Phi_2=0. \tag{3.2}$$

One can refer to our previous paper in [13] for the equations that are used to govern the introduced two correction potentials (or Lagrange multipliers) Φ_1 and Φ_2.

Another way that differs from the explicit cleaning method given in [13] will be adopted in this paper to compensate for the omission of two Gauss equations (3)-(4). Take the electric field as an example, we know that the value of $\underline{E}$ calculated from the Faraday's equations are in general not divergence-free. One can, thus, express the computed electric field vector as the sum of $-\nabla\phi$ and $\nabla\times\underline{V}$, where ϕ denotes the scalar

function and $\underline{V}$ is the vector function. Decomposition of the solution in this way enables us to correct the electric field by means of $\underline{E}_c = \underline{E} + \nabla\phi$ so as to make the corrected vector field $\underline{E}_c$ to be solenoidal.

By performing the divergence operator $(\nabla\cdot)$ on both hand sides of $\underline{E}_c = \underline{E} + \nabla\phi_E$, the equation for the correction potential in Ω can be obtained as

$$\nabla^2\phi_E = -\nabla\cdot\underline{E}. \tag{3.3}$$

Given the computed values of $\underline{E}$ from the Faraday's equations, the above equation for ϕ will be solved subject to the zero boundary condition specified along the boundary $\partial\Omega$ since the Lagrange multiplier is simply used to enforce the divergence-free condition. Note that ϕ_E is prescribed to be zero along the boundary since its primary role is to ensure stability [14]. One can adopt the similar idea to correct the solution by adding $\nabla\phi_H$, where ϕ_H is governed by $\nabla^2\phi_H = -\nabla\cdot\underline{H}$ in Ω and $\phi_H = 0$ is prescribed along $\partial\Omega$, to the magnetic field solution $\underline{E}$ that is computed from the Ampère's law.

4 Discretization method

For easily describing the proposed discretization scheme, we choose the two-dimensional Maxwell's equations in Cartesian coordinate system. In the case of transverse magnetic (TM) polarization, the time-evolving magnetic vector field variables $(H_x, H_y, 0)$ and the electric scalar field variable E_z are governed by the following three equations

$$\frac{\partial H_x}{\partial t} = -\frac{1}{\mu}\frac{\partial E_z}{\partial y}, \tag{4.1a}$$

$$\frac{\partial H_y}{\partial t} = \frac{1}{\mu}\frac{\partial E_z}{\partial x}, \tag{4.1b}$$

$$\frac{\partial E_z}{\partial t} = \frac{1}{\epsilon}\left(\frac{\partial H_y}{\partial x} - \frac{\partial H_x}{\partial y}\right). \tag{4.1c}$$

The quality of the TM-mode solutions predicted from the above equations depends partly on the applied discretization scheme for the first-order spatial derivative terms and partly on the temporal scheme used to approximate the time derivative term. We will start with the scheme development for the temporal derivative terms and, then, the scheme development in Section 5.2 for the spatial derivative terms shown in (4.1).

The most frequently applied time domain method in computational electromagnetics was originally proposed by Yee [2]. This finite difference method was formulated on the staggered mesh, upon which the electric and magnetic field variables are stored at different locations. While such a storage of electric and magnetic fields makes the boundary treatment easier, it suffers from a strict stability condition.

One can only find very few non-staggered Maxwell's equation solvers in the literature. In dense grids, Pinho et al. [15] solved the Maxwell's equations in non-staggered

grids by using the interpolating wavelets to get the substantial gains in memory and speed. Another numerical study of the Maxwell's equations on non-staggered grids was due to Liu [16] who assessed the finite difference solutions computed on the non-staggered, collocated staggered, and the non-collocated staggered grids by applying the Fourier method to analyze the predicted dispersive, dissipative and isotropic errors. While the non-collocated staggered grid has the most favorable property [16], we adopt in this study the non-staggered grid approach since it is programmingly more simple and is more applicable to parallel computing. In non-staggered (or collocated) grids, to avoid the undesirable oscillatory solution arising from the even-odd or checkerboard decoupling, we have applied the concept of compact scheme [13] to successfully resolve the oscillatory problem. In the finite volume context, Maxwell's equations have been discretized in non-staggered mesh by Munz et al. [17].

4.1 Explicit symplectic partitioned Runge-Kutta scheme

Faraday's and Ampère's equations shown in (2.1)-(2.2) constitute a Hamiltonian differential system since they can be expressed in terms of the Hamiltonian function H, defined in (2.13), as follows

$$\frac{\partial \underline{E}}{\partial t} = \frac{\delta H}{\partial \underline{H}}, \tag{4.2}$$

$$\frac{\partial \underline{H}}{\partial t} = -\frac{\delta H}{\partial \underline{E}}. \tag{4.3}$$

Because of the above infinite dimensional Hamiltonian system of canonical equations, one should numerically integrate them using the symplectic integrators to retain their long-term solution behavior.

Two major types of symplectic integrators are available for choice [18]. One of them was developed by properly choosing the generating functions. The other group of the symplectic integrators consists of, for example, the Runge-Kutta, Runge-Kutta-Nyström and partitioned Runge-Kutta methods. Note that the symplectic Runge-Kutta-Nyström time integrator and the partitioned Runge-Kutta time integrator, which is applicable to the separable Hamiltonian system, can be developed within an implicit or an explicit context [18].

To preserve symplectic structure and conserve total energy in the investigated Maxwell's equations, the implicit or explicit symplectic methods should be chosen. In addition to preserving the symplectic structure along the time direction, we are also aimed to develop a dispersively very accurate scheme in the spatial directions. Our strategy to get a higher spatial accuracy is to make the numerical dispersion relation equation for the Maxwell's equations closer to their exact dispersion relation equation. In the wavenumber space, we will therefore derive the numerical angular frequency explicitly in terms of the wave numbers in x and y directions. It is difficult or almost impossible to apply any implicit symplectic Runge-Kutta scheme, which comprises the coupled solution

steps [19], to derive the numerical dispersion relation equation [18]. We will therefore employ in this study the explicit symplectic Runge-Kutta scheme. Our goal is to minimize the difference between the exact and numerical dispersion relation equations for the separable Hamiltonian system of Maxwell's equations.

Maxwell's equations can be rewritten into the following infinite dimensional Hamiltonian system which is endowed with the Hamiltonian H. We can, as a result, write the separable Hamiltonian function H as $T(\underline{E})+V(\underline{H})$, which is the energy density. Since the Hamiltonian system of Maxwell's equations is separable, we can now apply the explicit symplectic partitioned Runge-Kutta time-stepping scheme to integrate this differential system of equations through the use of two introduced tableaus for the respective Faraday's and Ampère's equations [18]. In this study, the second-order accurate explicit partitioned Runge-Kutta scheme given in [20] is adopted to approximate the time derivative terms. The resulting semi-discretized equations are read as

$$\underline{H}^* = \underline{H}^n - \frac{dt}{2\mu}\nabla\times\underline{E}^n, \tag{4.4a}$$

$$\underline{E}^{n+1} = \underline{E}^n + \frac{dt}{\epsilon}\nabla\times\underline{H}^*, \tag{4.4b}$$

$$\underline{H}^{n+1} = \underline{H}^* - \frac{dt}{2\mu}\nabla\times\underline{E}^{n+1}. \tag{4.4c}$$

Discretization of the Maxwell's equations proceeds as usual by performing approximation on the remaining first-order derivative terms shown in (4.4).

4.2 Discretization of one-dimensional Ampère's and Faraday's equations

Since the first-order Ampère's and Faraday's equations can be transformed respectively to their equivalent second-order equations, which are

$$\frac{\partial^2\underline{E}}{\partial t^2} = \frac{1}{\epsilon\mu}\nabla^2\underline{E}, \qquad \frac{\partial^2\underline{H}}{\partial t^2} = \frac{1}{\epsilon\mu}\nabla^2\underline{H}, \tag{4.5}$$

the spatial derivative terms for $\underline{E}$ and $\underline{H}$, which are $\frac{\partial E_z}{\partial x}$ and $\frac{\partial H_y}{\partial x}$ in the TM-mode equations shown in (4.1), should be approximated by a center-type numerical scheme. We first approximate the semi-discretized one-dimensional Faraday's equation by $\underline{H}^* = \underline{H}^n - \frac{dt}{2\mu}\nabla\times\underline{E}^n$. The physically correct space-centered scheme for the term $\frac{\partial E_z}{\partial x}$ at an interior point i in a uniform grid system of mesh size Δx involves using the following six stencil points $i\pm1$, $i\pm2$, $i\pm3$:

$$\left.\frac{\partial E_z}{\partial x}\right|_i = \frac{1}{\Delta x}\Big[a_1\left(E_z|_{i+3}-E_z|_{i-3}\right)+a_2\left(E_z|_{i+2}-E_z|_{i-2}\right)+a_3\left(E_z|_{i+1}-E_z|_{i-1}\right)\Big]. \tag{4.6}$$

The other first-order spatial derivative term $\frac{\partial H_y}{\partial x}$ is approximated by the same centered scheme as that shown in (4.6).

By substituting the centered approximated equation for $\frac{\partial E_z}{\partial x}|^n$ into Eq. (4.4a) and then plugging the resulting magnetic field solution $\underline{H}^*$ into Eq. (4.4b), we can get the following equation for the one-dimensional Ampère's equation by virtue of the equations $\underline{H}^n=\underline{H}^0-\frac{dt}{2\mu}\nabla\times\underline{E}^n$ and $\nabla\times\underline{H}^0=\frac{\varepsilon}{\Delta t}\left(\underline{E}^n-\underline{E}^{n-1}\right)$

$$\begin{aligned}E_z|_i^{n+1}=&2E_z|_i^n-E_z|_i^{n-1}+\frac{c^2\Delta t^2}{\Delta x^2}\Big[a_1^2\left(E_z|_{i+6}^n+E_z|_{i-6}^n\right)\\&+2a_1a_2\left(E_z|_{i+5}^n+E_z|_{i-5}^n\right)+\left(2a_1a_3+a_2^2\right)\left(E_z|_{i+4}^n+E_z|_{i-4}^n\right)\\&+2a_2a_3\left(E_z|_{i+3}^n+E_z|_{i-3}^n\right)-a_3\left(2a_1-a_3\right)\left(E_z|_{i+2}^n+E_z|_{i-2}^n\right)\\&-2a_2\left(a_1+a_3\right)\left(E_z|_{i+1}^n+E_z|_{i-1}^n\right)-2\left(a_1^2+a_2^2+a_3^2\right)E_z|_i^n\Big].\end{aligned}\tag{4.7}$$

Following the same procedures as did before for the discretization of Ampère's equation, the algebraic equation for the Faraday's equation can be also derived as follows

$$\begin{aligned}H_y|_i^{n+1}=&2H_y|_i^n-H_y|_i^{n-1}+\frac{c^2\Delta t^2}{\Delta x^2}\Big[a_1^2\left(H_y|_{i+6}^n+H_y|_{i-6}^n\right)\\&+2a_1a_2\left(H_y|_{i+5}^n+H_y|_{i-5}^n\right)+\left(2a_1a_3+a_2^2\right)\left(H_y|_{i+4}^n+H_y|_{i-4}^n\right)\\&+2a_2a_3\left(H_y|_{i+3}^n+H_y|_{i-3}^n\right)-a_3\left(2a_1-a_3\right)\left(H_y|_{i+2}^n+H_y|_{i-2}^n\right)\\&-2a_2\left(a_1+a_3\right)\left(H_y|_{i+1}^n+H_y|_{i-1}^n\right)-2\left(a_1^2+a_2^2+a_3^2\right)H_y|_i^n\Big].\end{aligned}\tag{4.8}$$

Note that the above equation is derived by using the following three equations

$$\underline{H}^n=\underline{H}^0-\frac{\Delta t}{2\mu}\nabla\times\underline{E}^n,\tag{4.9}$$

$$\underline{E}^n=\underline{E}^{n-1}+\frac{\Delta t}{\epsilon}\nabla\times\underline{H}^0,\tag{4.10}$$

$$\underline{H}^0=\underline{H}^{n-1}-\frac{\Delta t}{2\mu}\nabla\times\underline{E}^{n-1}.\tag{4.11}$$

We need now to determine the free parameters a_1, a_2 and a_3 shown in Eqs. (4.7) and (4.8) to close the system of the discrete Maxwell's equations. Our aim is to rigorously derive a system of three algebraic equations for a_1, a_2 and a_3 for getting a good overall accuracy. Our strategy is to reduce the amplitude as well as the phase errors generated from the discretized Ampère's and Faraday's equations. We perform first the modified equation analysis on Eq. (4.10) by expanding the terms $H_{i\pm3}$, $H_{i\pm2}$, $H_{i\pm1}$ in Taylor series with respect to H_i. The leading two discretization errors shown in the resulting derived

modified equation are then eliminated to get the following two algebraic equations

$$3a_1+2a_2+a_3=\frac{1}{2}, \tag{4.12}$$

$$27a_1+8a_2+a_3=0. \tag{4.13}$$

One more algebraic equation needs to be derived for the closure reason.

To retain the propagation characteristics of the TM-mode Maxwell's equations, we need to, in particular, reduce the error of dispersion type. The reason is that such an error can cause the phase velocity to be the function of frequency and propagation angle. While only a small error is generated in the wave propagation velocity, phase error may cumulate to an unacceptable amount, thereby posing limitations on the long-term simulation carried out in a large domain. Another problem associated with the numerical dispersion error is the unphysical refraction [21]. In [22], one can find several methods proposed in the past to reduce the dispersion error.

Dispersion relation connects the angular frequency ω of the wave with the wavenumber k. It is the equation for which the plane wave in the form of $e^{\underline{k}\cdot\underline{x}-I\omega(k)t}$ solves the equation. A higher dispersion accuracy can be obtained provided that the numerical angular frequency for the differential system of Ampère's and Faraday's equations relates well with the wavenumbers. Our strategy of deriving the last algebraic equation is to develop a scheme whose numerical dispersion relation equation agrees well with its exact dispersion relation equation. To achieve this goal, we will transform the equation in the space-time domain (x,t) to its corresponding angular frequency-wavenumber space (ω,k_x).

By substituting first the following plane-wave solution for E_z, which is

$$E_z|_i^n=E_z^0e^{I(\omega n\Delta t-k_xi\Delta x)}, \tag{4.14}$$

and the plane wave solution for H_y, which is

$$H_y|_i^n=H_y^0e^{I(\omega n\Delta t-k_xi\Delta x)}, \tag{4.15}$$

into the differential equation (4.7) or (4.8), the following equation can be derived

$$\begin{aligned}e^{I\omega\Delta t}-2+e^{-I\omega\Delta t}=\frac{c^2\Delta t^2}{\Delta x^2}\Bigg[&a_1^2\left(e^{6Ik_x\Delta x}+e^{-6Ik_x\Delta x}\right)+2a_1a_2\left(e^{5Ik_x\Delta x}+e^{-5Ik_x\Delta x}\right)\\&+\left(2a_1a_3+a_2^2\right)\left(e^{4Ik_x\Delta x}+e^{-4Ik_x\Delta x}\right)+2a_2a_3\left(e^{3Ik_x\Delta x}+e^{-3Ik_x\Delta x}\right)\\&-a_3\left(2a_1-a_3\right)\left(e^{2Ik_x\Delta x}+e^{-2Ik_x\Delta x}\right)-2a_2\left(a_1+a_3\right)\left(e^{Ik_x\Delta x}+e^{-Ik_x\Delta x}\right)\\&-2\left(a_1^2+a_2^2+a_3^2\right)\Bigg].\end{aligned} \tag{4.16}$$

One can then get the following numerical dispersion relation equation for the one-dimensional Ampère's and Faraday's equations

$$\omega_{num}\Delta t=\cos^{-1}\left[\frac{c^2\Delta t^2}{\Delta x^2}\left(a_1^2\cos(6k_x\Delta x)+2a_1a_2\cos(5k_x\Delta x)+\left(2a_1a_3+a_2^2\right)\cos(4k_x\Delta x)\right.\right.$$
$$+2a_2a_3\cos(3k_x\Delta x)-a_3(2a_1-a_3)\cos(2k_x\Delta x)$$
$$\left.\left.-2a_2(a_1+a_3)\cos(k_x\Delta x)-\left(a_1^2+a_2^2+a_3^2\right)+1\right)\right]. \tag{4.17}$$

Before performing minimization, we need to know the analytic dispersion relation equation for the one-dimensional Maxwell's equations. The following equation relates the exact angular frequency ω_{exact} with the wave number k_x.

$$\omega_{exact}^2=k_x^2c^2. \tag{4.18}$$

For getting a dispersive accuracy as high as possible, we minimize the difference between the exact group velocity $\frac{\partial\omega_{exact}}{\partial k_x}$ and the numerical group velocity $\frac{\partial\omega_{num}}{\partial k_x}$. Following this line of thought, we define first the error function as $\left[\frac{\partial\omega_{num}}{\partial k_x}-\frac{\partial\omega_{exact}}{\partial k_x}\right]^2$. This error function is then minimized in the weak sense within the integral range of $-m\pi\leq hk_x\leq m\pi$

$$E=\int_{-m\pi}^{m\pi}\left[\frac{\partial\omega_{num}}{\partial k_x}-\frac{\partial\omega_{exact}}{\partial k_x}\right]^2W(\gamma)\,d\gamma. \tag{4.19}$$

In the above, $\gamma=hk_x$ denotes the scaled wavenumber and $W(\gamma)$ is known as the weighting function. Inclusion of the weighting function in the process of minimization enables us to analytically integrate Eq. (4.19).

To avoid the aliasing error, the factor m, whose value falls between 0 and $\frac{1}{2}$, is also included so as to determine the optimized range. Besides the above two guidelines of constructing the error function, a properly designed object function for the minimization purpose should be applicable to a region of higher wavenumber (or closer to π) where the dispersive error prevails. According to the work of Kim and Lee [23], we can introduce also the exponential function $\exp(\gamma)$ and multiply it with the integrand in (4.19) to yield another weighting function. While inclusion of this exponential function helps to reduce the dispersive error in a high wavenumber range, for simplicity we don't take this exponential function into account in this study.

The error function E will be minimized by enforcing the limiting condition given by $\frac{\partial E}{\partial a_3}=0$ to get the third algebraic equation. The equation derived from this minimizing procedure will be used together with the other two algebraic equations that were derived previously from the modified equation analysis. Through the simulation results tabulated in Table 1, the best result is obtained at $m=\frac{1}{2}$. The resulting three introduced coefficients a_i ($i=1\sim3$) in Eq. (4.6) are $a_1=0.024209$, $a_2=-0.18017$, $a_3=0.78771$. Through

Table 1: Comparison of the L_2-error norms for E_z obtained at different integration parameters m at $t=10$ in a domain of 201^2 mesh points.

Integration parameter m	L_2-**error norm of** E_z
1/2	2.2340E-04
3/7	5.5748E-04
2/5	3.5673E-04
1/3	6.1732E-04

Table 2: Comparison of the computed L_2-error norms and the required CPU times for the two schemes carried out at $t=10$ in 41^2,51^2,61^2 and 71^2 four meshes.

	L_2-**error norm**		**CPU time (s)**	
	Present	Yee [2]	Present	Yee [2]
41×41	1.0933E-02	0.1478	1.4375	0.1875
51×51	5.2251E-03	9.2943E-02	3.3125	0.3594
61×61	3.0854E-03	6.3856E-02	5.0625	0.6094
71×71	2.0131E-03	4.6592E-02	7.2188	0.9688

Table 3: Comparison of the required CPU times for the two investigated schemes, which yield approximately the same L_2-error norm, at time $t=10$.

Present			**Yee [2]**		
L_2-error norm	Grid	CPU time (s)	L_2-error norm	Grid	CPU time (s)
1.0933E-02	41×41	1.4375	1.5649E-02	121×121	4.6719
5.2251E-03	51×51	3.3125	6.3570E-03	189×189	19.0937
3.0854E-03	61×61	5.0625	3.1511E-03	268×268	56.5937

the minimization procedure performed in the wavenumber space and the modified equation analysis for $\frac{\partial H_x}{\partial x}$, we know that the proposed space centered scheme with the best numerical dispersion relation equation has the spatial accuracy order of fourth

$$\frac{\partial H_x}{\partial x}=\frac{\partial H_x}{\partial x}\Big|_{exact}-0.015115h^4\frac{\partial^5 H_x}{\partial x^5}+\mathcal{O}(h^6)+\cdots. \tag{4.20}$$

Fundamental analysis of the proposed spatial scheme starts from defining the coefficients k_i and k_r for the respective dispersion and dissipation errors as $k_i=\Re[\tilde{\alpha}\Delta x]$ and $k_r=\Im[\tilde{\alpha}\Delta x]$. $\Re[\tilde{\alpha}\Delta x]$ denotes the real part of $\tilde{\alpha}\Delta x$ and $\Im[\tilde{\alpha}\Delta x]$ stands for the imaginary part of $\tilde{\alpha}\Delta x$ of the proposed scheme. It is worthy to note that k_r is always equal to zero due to the chosen symmetric stencil points in the current space-centered scheme. In Fig. 1, the values of k_i are plotted against the modified wavenumber at different values of C_r ($\equiv\frac{c\Delta t}{\Delta x}$). For the sake of comparison, we also plot the values of k_i for the schemes of Tam and Webb [24], Lele [25], and Bogry and Bally [26]. For completeness, the numerical angular frequency ω_{num} is also plotted against the wavenumber κ in Fig. 2 at different values of the Courant number C_r.

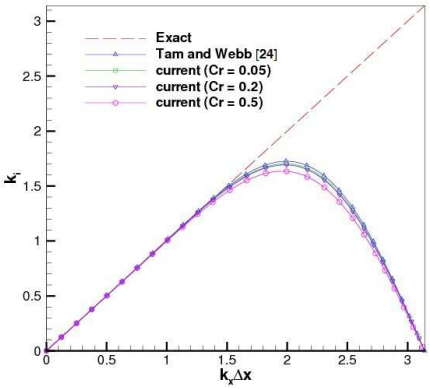

Figure 1: Comparison of the computed values of k_i against the modified wavenumber $k_x\Delta x$ using the present and the scheme of Tam and Webb [24] at three chosen Courant numbers.

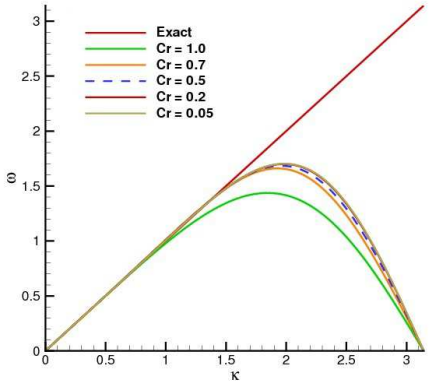

Figure 2: Plot of the angular frequencies ω against wavenumber k at different values of C_r $(\equiv \frac{c\Delta t}{\Delta x}) =$ 0.05, 0.2, 0.5, 0.7 and 1.0.

5 Discretization of two-dimensional Ampère's and Faraday's equations

We first approximate the time derivative term to get the semi-discretized Faraday's equation

$$\underline{H}^* = \underline{H}^n - \frac{dt}{2\mu}\nabla \times \underline{E}^n. \tag{5.1}$$

The physically correct space-centered scheme is then applied to approximate the spatial terms $\frac{\partial E_z}{\partial x}$ and $\frac{\partial E_z}{\partial y}$ at an interior point (i,j) in a uniform grid system of mesh size $\Delta x = \Delta y$. This center scheme involves using the nodal solutions at the stencil points $(i\pm1,j)$, $(i\pm2,j)$, $(i\pm3,j)$, $(i,j\pm1)$, $(i,j\pm2)$ and $(i,j\pm3)$ as follows:

$$\frac{\partial E_z}{\partial x}|_{i,j} = \frac{1}{\triangle x}\left[a_1\left(E_z|_{i+3,j} - E_z|_{i-3,j}\right) + a_2\left(E_z|_{i+2,j} - E_z|_{i-2,j}\right) + a_3\left(E_z|_{i+1,j} - E_z|_{i-1,j}\right)\right], \tag{5.2a}$$

$$\frac{\partial E_z}{\partial y}|_{i,j} = \frac{1}{\triangle y}\left[a_1\left(E_z|_{i,j+3} - E_z|_{i,j-3}\right) + a_2\left(E_z|_{i,j+2} - E_z|_{i,j-2}\right) + a_3\left(E_z|_{i,j+1} - E_z|_{i,j-1}\right)\right]. \tag{5.2b}$$

Other first-order spatial derivative terms $\frac{\partial H_y}{\partial x}$ and $\frac{\partial H_x}{\partial y}$ can be approximated using the same space-centered schemes as those shown in (5.2).

By substituting the above space-centered equation for $\frac{\partial E_z}{\partial x}|^n$ into Eq. (4.4a) and then the magnetic field solution $\underline{H}^*$ into Eq. (4.4b), one can get the two-dimensional discretized

equation for E_z by virtue of $\underline{H}^n=\underline{H}^0-\frac{\Delta t}{2\mu}\nabla\times\underline{E}^n$ and $\nabla\times\underline{H}^0=\frac{\varepsilon}{\Delta t}\left(\underline{E}^n-\underline{E}^{n-1}\right)$

$$\begin{aligned}E_z|_{i,j}^{n+1}=&2E_z|_{i,j}^{n}-E_z|_{i,j}^{n-1}+\frac{c^2\Delta t^2}{\Delta x^2}\Bigg[a_1^2\left(E_z|_{i+6,j}^{n}+E_z|_{i-6,j}^{n}\right)+2a_1a_2\left(E_z|_{i+5,j}^{n}+E_z|_{i-5,j}^{n}\right)\\&+\left(2a_1a_3+a_2^2\right)\left(E_z|_{i+4,j}^{n}+E_z|_{i-4,j}^{n}\right)+2a_2a_3\left(E_z|_{i+3,j}^{n}+E_z|_{i-3,j}^{n}\right)\\&-a_3\left(2a_1-a_3\right)\left(E_z|_{i+2,j}^{n}+E_z|_{i-2,j}^{n}\right)-2a_2\left(a_1+a_3\right)\left(E_z|_{i+1,j}^{n}+E_z|_{i-1,j}^{n}\right)\\&-2\left(a_1^2+a_2^2+a_3^2\right)E_z|_{i,j}^{n}\Bigg]+\frac{c^2\Delta t^2}{\Delta y^2}\Bigg[a_1^2\left(E_z|_{i,j+6}^{n}+E_z|_{i,j-6}^{n}\right)\\&+2a_1a_2\left(E_z|_{i,j+5}^{n}+E_z|_{i,j-5}^{n}\right)+\left(2a_1a_3+a_2^2\right)\left(E_z|_{i,j+4}^{n}+E_z|_{i,j-4}^{n}\right)\\&+2a_2a_3\left(E_z|_{i,j+3}^{n}+E_z|_{i,j-3}^{n}\right)-a_3\left(2a_1-a_3\right)\left(E_z|_{i,j+2}^{n}+E_z|_{i,j-2}^{n}\right)\\&-2a_2\left(a_1+a_3\right)\left(E_z|_{i,j+1}^{n}+E_z|_{i,j-1}^{n}\right)-2\left(a_1^2+a_2^2+a_3^2\right)E_z|_{i,j}^{n}\Bigg].\end{aligned}\tag{5.3}$$

Numerical dispersion relation equation for the differential system of two-dimensional Ampère's and Faraday's equations can be similarly derived by substituting the plane wave solutions $E_z|_i^n=E_z^0e^{I(\omega n\Delta t-k_xi\Delta x-k_yj\Delta y)}$, $H_x|_i^n=H_x^0e^{I(\omega n\Delta t-k_xi\Delta x-k_yj\Delta y)}$ and $H_y|_i^n=H_y^0e^{I(\omega n\Delta t-k_xi\Delta x-k_yj\Delta y)}$ into the above discrete equation. The following numerical dispersion relation equation can then be derived for the truly two-dimensional TM-mode Maxwell's equations

$$\begin{aligned}\omega_{num}\Delta t=\cos^{-1}\Bigg[&\frac{c^2\Delta t^2}{\Delta x^2}\Bigg(a_1^2\cos\left(6k_x\Delta x\right)+2a_1a_2\cos\left(5k_x\Delta x\right)+\left(2a_1a_3+a_2^2\right)\cos\left(4k_x\Delta x\right)\\&+2a_2a_3\cos\left(3k_x\Delta x\right)-a_3\left(2a_1-a_3\right)\cos\left(2k_x\Delta x\right)-2a_2\left(a_1+a_3\right)\cos\left(k_x\Delta x\right)\\&-\left(a_1^2+a_2^2+a_3^2\right)\Bigg)+\frac{c^2\Delta t^2}{\Delta y^2}\Bigg(a_1^2\cos\left(6k_y\Delta y\right)+2a_1a_2\cos\left(5k_y\Delta y\right)\\&+\left(2a_1a_3+a_2^2\right)\cos\left(4k_y\Delta y\right)+2a_2a_3\cos\left(3k_y\Delta y\right)-a_3\left(2a_1-a_3\right)\cos\left(2k_y\Delta y\right)\\&-2a_2\left(a_1+a_3\right)\cos\left(k_y\Delta y\right)-\left(a_1^2+a_2^2+a_3^2\right)\Bigg)+1\Bigg].\end{aligned}\tag{5.4}$$

The same procedure as that used in Section 4 is then applied to minimize the difference between the two-dimensional exact and numerical dispersion relation equations. Define the error function as follows

$$E=\int_{-m\pi}^{m\pi}\int_{-m\pi}^{m\pi}W(k_x\Delta x,\,k_y\Delta y)\left[\frac{\partial\omega_{num}}{\partial k}-\frac{\partial\omega_{exact}}{\partial k}\right]^2d(k_x\Delta x)\,d(k_y\Delta y).\tag{5.5}$$

The above real-valued error function has the minimum value, which is zero, provided that $\frac{\partial E}{\partial a_3}=0$. This error minimization provides us one algebraic equation for use to close the algebraic system for the determination of the three introduced parameters, which are $a_1=0.022277$, $a_2=-0.17244$ and $a_3=0.77805$, derived at $Cr=0.2$ and $m=\frac{1}{2}$.

Given the definition of $k^2=k_x^2+k_y^2$, we can write k_x and k_y in terms of the spherical coordinates k and θ as $k_x=k\cos\theta$ and $k_y=k\sin\theta$. For the sake of comparison and discussion of the computed results, two extra parameters $N_\lambda=\frac{\lambda}{h}$, which represents the number of points per wavelength λ $(=\frac{2\pi}{k})$, and $S=\frac{c\Delta t}{h}$, which is known as the CFL number, are defined. The speed of light c is chosen as the referenced speed and $h=\Delta x=\Delta y$ as the uniform grid size. Given the above two definitions, we can now proceed to derive the numerical phase velocity V_p, which is defined as the ratio of the numerical angular frequency and the wavenumber k. We can express $e^{I\omega_{num}\Delta t}$ by means of Eq. (5.4) to get

$$e^{I\omega\Delta t}=e^{I\Delta t(\omega_R+I\omega_I)}=e^{-\omega_I\Delta t}(\cos(\omega_R\Delta t)+I\sin(\omega_R\Delta t)). \tag{5.6}$$

Define $\hat{R}=e^{-\omega_I\Delta t}\cos(\omega_R\Delta t)$ and $\hat{I}=e^{-\omega_I\Delta t}\sin(\omega_R\Delta t)$, we can get $tan(\omega_R\Delta t)=\frac{\hat{I}}{\hat{R}}$ and, then, the ratio of numerical phase velocity $V_p=\frac{\omega_R}{k}$ to the exact phase velocity c [27]

$$\frac{V_p}{c}=\frac{\omega_R}{ck}=\frac{N_\lambda}{2\pi S}tan^{-1}\Big(\frac{\hat{I}}{\hat{R}}\Big). \tag{5.7}$$

For the sake of comparison, the ratio of the derived numerical phase velocity to the exact phase velocity $\frac{V_p}{c}$ are plotted for the three schemes investigated at different values of N_λ in Fig. 3. In the case of fewer number of grid points per wavelength, our scheme is clearly seen to give a better phase velocity. Also, all schemes are seen to perform better in the region near $\theta=45^\circ$. As the value of N_λ increases, the numerical phase velocity asymptotically approaches the exact phase velocity. For the sake of completeness, we also plot in Fig. 4 the free parameters a_1, a_2 and a_3 against the angle θ for the current scheme performed at different Courant numbers.

6 Implementation of boundary condition

Constitutive equations $\underline{B}=[\mu^*]\,\underline{H}$ and $\underline{D}=[\epsilon^*]\,\underline{E}$ describe the response of a medium to the electromagnetic field, where the tensors $[\mu^*]$ and $[\epsilon^*]$ are generally defined as $[\epsilon^*]=[\epsilon]+\frac{[\sigma_E]}{I\omega}$ and $[\mu^*]=[\mu]+\frac{[\sigma_M]}{I\omega}$, respectively. We denote $[\epsilon]$, $[\mu]$, $[\sigma_E]$ and $[\sigma_M]$ as the electric permittivity, magnetic permeability, electric conductivity, and magnetic conductivity tensors, respectively. The impedance of the chosen UPML should match that of the free space in the sense that $\epsilon_0^{-1}\mu_0=[\epsilon^*]^{-1}[\mu^*]$. This impedance matching assumption implies $\frac{[\epsilon^*]}{\epsilon_0}=\frac{[\mu^*]}{\mu_0}=[S]$. Adjacent to the domain of a scatter field, the absorbing layer for the mitigation of spurious wave reflections is characterized by the constitutive tensor $[S]$. As is well known in [28] that this perfectly matched anisotropic layer is recommended for

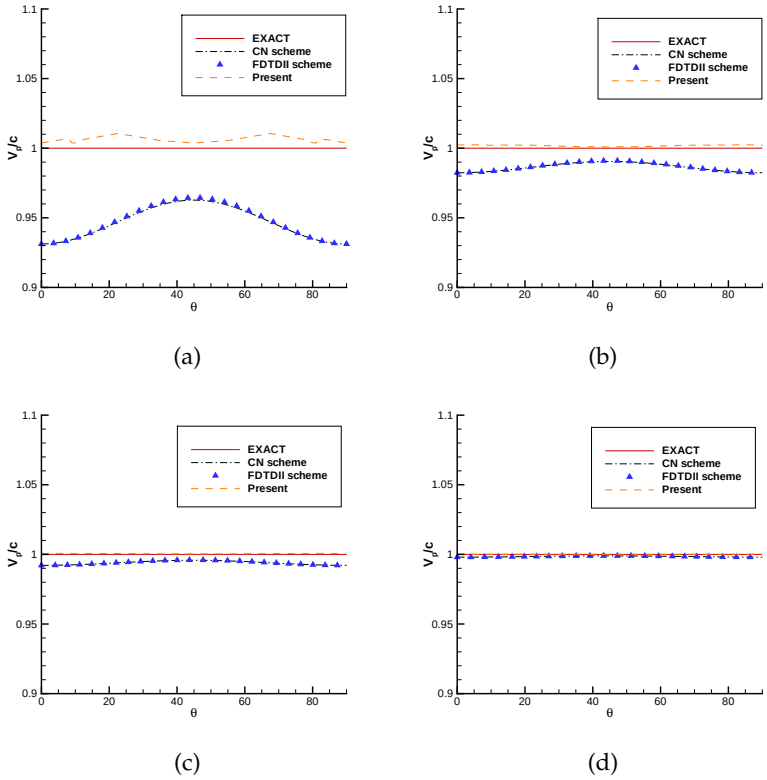

Figure 3: Comparison of the phase velocity ratios $\frac{V_p}{c}$ against θ at different N_λ using the CN [27], FDTDII [27] and the current schemes. (a) $N_\lambda=5$; (b) $N_\lambda=10$; (c) $N_\lambda=15$; (d) $N_\lambda=30$.

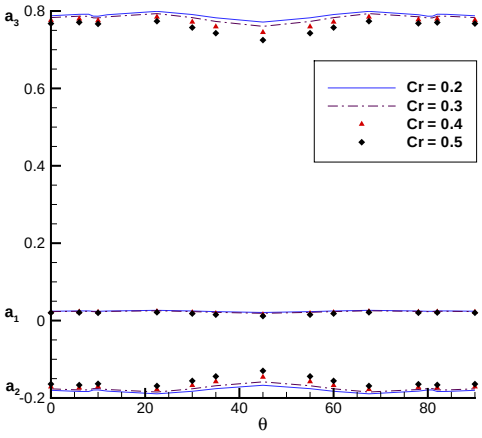

Figure 4: Plot of the free parameters a_1, a_2 and a_3 against the propagation angle θ ranging from 0° to 90° for the cases investigated at Cr= 0.2, 0.3, 0.4 and 0.5.

use as a substitution of the absorbing boundary condition. We adopt therefore the constitutive law given by $[S]=[S]_x[S]_y[S]_z$ for the purpose of attenuating the electromagnetic wave along the x, y, z directions, respectively. The three diagonal tensors are given by

$$[S]_x=\begin{bmatrix} S_x^{-1} & 0 & 0 \\ 0 & S_x & 0 \\ 0 & 0 & S_x \end{bmatrix}, \tag{6.1a}$$

$$[S]_y=\begin{bmatrix} S_y & 0 & 0 \\ 0 & S_y^{-1} & 0 \\ 0 & 0 & S_y \end{bmatrix}, \tag{6.1b}$$

$$[S]_z=\begin{bmatrix} S_z & 0 & 0 \\ 0 & S_z & 0 \\ 0 & 0 & S_{z^{-1}} \end{bmatrix}. \tag{6.1c}$$

The components in these constitutive tensors are represented by [29]

$$s_{\alpha(\alpha=x,y,z)}=1+\frac{\sigma_{\max}|\alpha-\alpha_0|^n}{I\omega\epsilon_0\delta^n} \tag{6.2}$$

for converting the frequency domain equations more easier to their time domain counterparts. Here, δ denotes the depth of the UPML layer. Based on our simulated results in Fig. 5, the value of n in the conductivity profile $\frac{\sigma_{\max}|\alpha-\alpha_0|^n}{\delta^n}$ is set at 3 since it yields an optimal absorption in the UPML. The location where $\alpha=\alpha_0$ is the interface between the UPML and the scatter field. In the constitutive tensor, $\sigma_{\max}$ is chosen as $\frac{(n+1)\ln(1/R_0)}{2\delta}$ [29], where $1/R_0=10^{16}$.

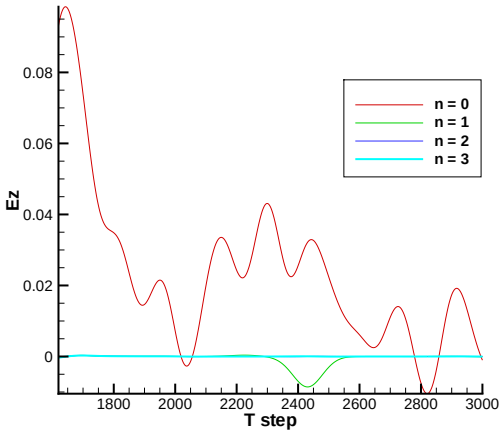

Figure 5: Comparison of the time-varying values of E_z at the point P $(x=336\ nm, y=0)$, schematic in Fig. 10, against the magnitudes of n in the conductivity profile $\frac{\sigma_{\max}|\alpha-\alpha_0|^n}{\delta^n}$.

Given the above constitutive equations, the Maxwell's equations in the absorbing layer for the mitigation of waves that may be possibly reflected from the truncated boundary are as follows:

$$\frac{\partial D_x}{\partial t}=\frac{\partial H_z}{\partial y}-\frac{\partial H_y}{\partial z}-\frac{\sigma_y}{\varepsilon_0}D_x, \qquad \frac{\partial D_y}{\partial t}=\frac{\partial H_x}{\partial z}-\frac{\partial H_z}{\partial x}-\frac{\sigma_z}{\varepsilon_0}D_y, \tag{6.3a}$$

$$\frac{\partial D_z}{\partial t}=\frac{\partial H_y}{\partial x}-\frac{\partial H_x}{\partial y}-\frac{\sigma_x}{\varepsilon_0}D_z, \qquad \frac{\partial B_x}{\partial t}=\frac{\partial E_y}{\partial z}-\frac{\partial E_z}{\partial y}-\frac{\sigma_y}{\varepsilon_0}B_x, \tag{6.3b}$$

$$\frac{\partial B_y}{\partial t}=\frac{\partial E_z}{\partial x}-\frac{\partial E_x}{\partial z}-\frac{\sigma_z}{\varepsilon_0}B_y, \qquad \frac{\partial B_z}{\partial t}=\frac{\partial E_x}{\partial y}-\frac{\partial E_y}{\partial x}-\frac{\sigma_x}{\varepsilon_0}B_z, \tag{6.3c}$$

$$\frac{\partial E_x}{\partial t}=\frac{1}{\varepsilon}\left(\frac{\partial H_z}{\partial y}-\frac{\partial H_y}{\partial z}-\frac{\sigma_y}{\varepsilon_0}D_x+\frac{\sigma_x}{\varepsilon_0}D_x\right)-\frac{\sigma_z}{\varepsilon_0}E_x, \tag{6.3d}$$

$$\frac{\partial E_y}{\partial t}=\frac{1}{\varepsilon}\left(\frac{\partial H_x}{\partial z}-\frac{\partial H_z}{\partial x}-\frac{\sigma_z}{\varepsilon_0}D_y+\frac{\sigma_y}{\varepsilon_0}D_y\right)-\frac{\sigma_x}{\varepsilon_0}E_y, \tag{6.3e}$$

$$\frac{\partial E_z}{\partial t}=\frac{1}{\varepsilon}\left(\frac{\partial H_y}{\partial x}-\frac{\partial H_x}{\partial y}-\frac{\sigma_x}{\varepsilon_0}D_z+\frac{\sigma_z}{\varepsilon_0}D_z\right)-\frac{\sigma_y}{\varepsilon_0}E_z, \tag{6.3f}$$

$$\frac{\partial H_x}{\partial t}=\frac{1}{\mu}\left(\frac{\partial E_y}{\partial z}-\frac{\partial E_z}{\partial y}-\frac{\sigma_y}{\varepsilon_0}B_x+\frac{\sigma_x}{\varepsilon_0}B_x\right)-\frac{\sigma_z}{\varepsilon_0}H_x, \tag{6.3g}$$

$$\frac{\partial H_y}{\partial t}=\frac{1}{\mu}\left(\frac{\partial E_z}{\partial x}-\frac{\partial E_x}{\partial z}-\frac{\sigma_z}{\varepsilon_0}B_y+\frac{\sigma_y}{\varepsilon_0}B_y\right)-\frac{\sigma_x}{\varepsilon_0}H_y, \tag{6.3h}$$

$$\frac{\partial H_z}{\partial t}=\frac{1}{\mu}\left(\frac{\partial E_x}{\partial y}-\frac{\partial E_y}{\partial x}-\frac{\sigma_x}{\varepsilon_0}B_z+\frac{\sigma_z}{\varepsilon_0}B_z\right)-\frac{\sigma_y}{\varepsilon_0}H_z. \tag{6.3i}$$

7 Numerical results

The explicit symplectic scheme with the optimized numerical dispersion relation equation derived in non-staggered grids will be validated by solving the TM-mode Maxwell's equations. In this study the problem amenable to analytic solution will be solved. This chosen problem solved at $\mu=1$ and $\epsilon=1$ in $-1\le x\le 1$ and $-1\le y\le 1$ has the initial solenoidal solutions $E_z(x,y,0)=\sin(3\pi x)\ \sin(4\pi y)$, $H_x(x,y,0)=-\frac{4}{5}\cos(3\pi x)\ \cos(4\pi y)$ and $H_y(x,y,0)=-\frac{3}{5}\sin(3\pi x)\ \sin(4\pi y)$. The exact electric and magnetic field solutions to Eqs. (2.1)-(2.2) take the following form [1]

$$E_z(x,y,t)=\sin(3\pi x-5\pi t)\ \sin(4\pi y), \tag{7.1a}$$

$$H_x(x,y,t)=-\frac{4}{5}\cos(3\pi x-5\pi t)\ \cos(4\pi y), \tag{7.1b}$$

$$H_y(x,y,t)=-\frac{3}{5}\sin(3\pi x-5\pi t)\ \sin(4\pi y). \tag{7.1c}$$

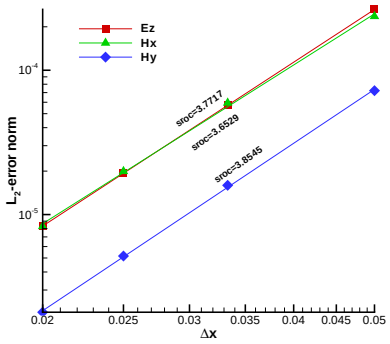

Figure 6: The computed L_2-error norms for the three TM-mode field variables and their corresponding spatial rates of convergence (sroc). The error norms are computed at $\Delta t = 1/5000$, $\Delta x = \Delta y = 1/20, 1/30, 1/40, 1/50$.

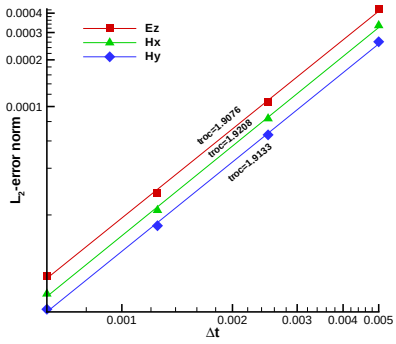

Figure 7: The computed L_2-error norms at $t = 0.1$ for the three TM-mode field variables and their corresponding temporal rates of convergence (troc). The error norms are computed at $\Delta x = \Delta y = 1/100$, $\Delta t = 1/200$, $1/400$, $1/800$, $1/1600$.

Besides performing the above validation study, we are also aimed to get the spatial and temporal rates of convergence for the proposed scheme. For this reason, we carry out calculations first at $\Delta t = 1/5000$, which is much smaller than the four chosen grid sizes $\Delta x = \Delta y = 1/20, 1/30, 1/40, 1/50$. The predicted errors cast in their L_2-error norms are plotted in Fig. 6, from which we know that the numerically predicted spatial rate of convergence is closed to the theoretical fourth-order accuracy. The second set of calculations performed at $\Delta x = \Delta y = 1/50$, which is smaller than the smallest time increments of $\Delta t = 1/18, 1/19, 1/20, 1/21$, enables us to get the temporal rate of convergence. As Fig. 7 shows, the L_2-error norm is decreased with the decreasing time interval Δt at an approximated theoretical rate of second.

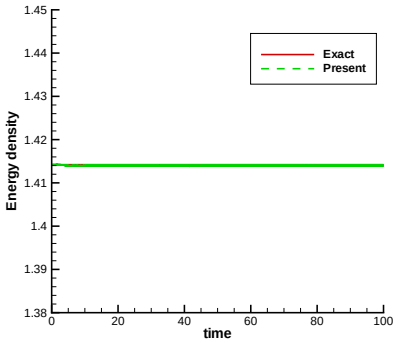

Figure 8: Comparison of the computed and exact energy densities, shown in (2.9), against time.

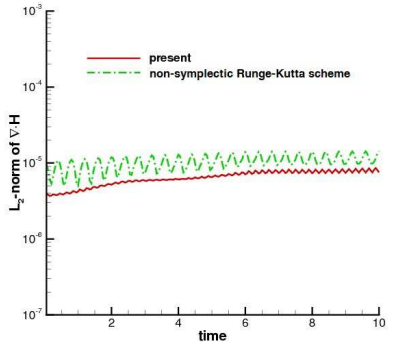

Figure 9: Comparison of the computed L_2-norms of $\nabla \cdot \underline{H}$ against time using the fourth-order non-symplectic Runge-Kutta scheme and the present explicit symplectic partitioned Runge-Kutta scheme.

For an additional justification of the proposed scheme, the Hamiltonian defined in (2.13) and the energy density given in (2.14) are calculated. Note that the Hamiltonian is trivially equal to zero in any two-dimensional TM-mode Maxwell's equations. As a result, only the predicted and exact energy densities are plotted against time in Fig. 8. One can clearly see from this figure that the computed W_1 and W_2 values do not change with time. We will also calculate the time-varying L_2-norms of $\nabla\cdot\underline{H}$ and plot them to examine if the Gauss's law is satisfied discretely. In Fig. 9, the magnetic field is indeed predicted to be divergence-free.

7.1 Mie scattering problem

In this study we will simulate the Mie scattering wave propagation in a two dimensional domain because of the available analytical solution [30]. Dielectric cylinder, which is known to be able to scatter the electromagnetic wave, with the diameter 126.56 nm is located at the center of a square of length 600 nm. This isotropic cylinder embedded in the homogeneous air medium has $\epsilon_r = 12.1104$ under the x-polarized plane wave incidence. This wave of amplitude 0.5 $\frac{v}{m}$ and angular frequency 13.263 $\frac{rad}{s}$ travels towards the positive x direction according to the one-dimensional Maxwell equations $\frac{\partial E_z}{\partial t} = \frac{1}{\epsilon}\nabla\times H$, $\frac{\partial H}{\partial t} = -\frac{1}{\mu}\nabla\times\underline{E}$.

In the presence of a dielectric cylinder in the physical interior, scattering wave patterns are inevitable. As a result, the total field/scattered field formulation will be adopted. As illustrated in Fig. 10, one can see that the physical domain is divided into three regions. The region for the total field encloses the dielectric cylinder whereas the scattered field region encloses the total field region. Note that only the scattered field components are stored in the scattered field. The third region that encloses the scattered field will be explained below.

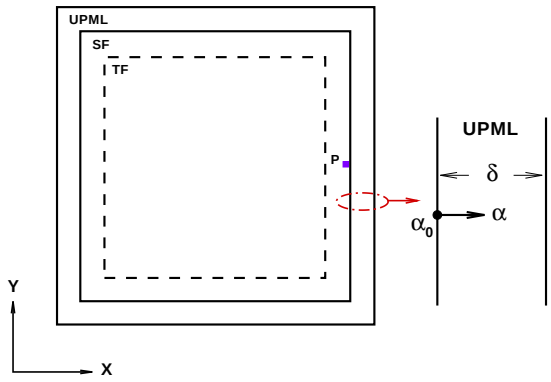

Figure 10: Schematic of the domain comprising the UPML and TF/SF three subdomains.

Most often, it is computationally infeasible to simulate waves scattered from the dielectric cylinder in free space. Because of this simulation limitation, Maxwell's equations

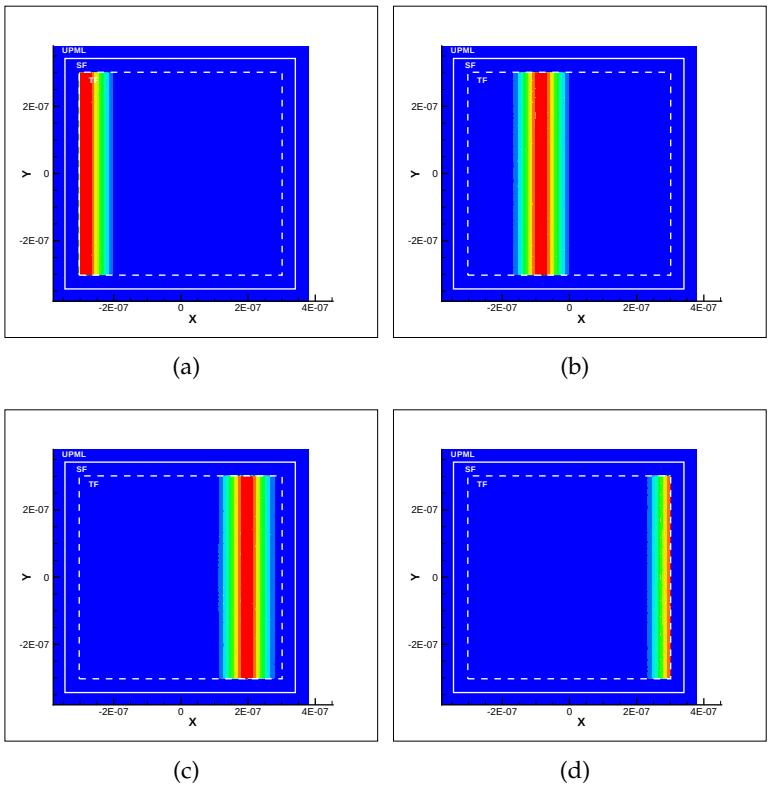

Figure 11: The predicted contour plots of E_z in TF/SF for the case without any scatter. (a) time step$=600$; (b) time step$=850$; (c) time step$=1200$; (d) time step$=1350$.

will be solved only in a finite domain. Under this circumstance, the fields on the truncated boundaries must be well defined so that the region appears to extend infinitely in all directions. The perfectly matched layer (PML) absorption boundary condition proposed by Berenger [31] will be adopted.

To check if the scattered waves will be reflected from the truncated boundaries, leading to an inaccurate result, we consider first the x-direction wave traveling from left to right. In Fig. 11, no wave was observed to reflect back to the physical domain of current interest. This demonstrates the proper application of the absorbing boundary condition. In the current study of the Mie scattering problem, our simulation was carried out by solving the Maxwell's equations given in (6.3) in a domain Ω $[-380,380]$ nm with the uniformly distributed mesh points at $Cr=0.2$, which corresponds to the time increment $\Delta t=0.0026685$ fs. The simulated time evolving contours for E_z schematic in Fig. 12 clearly exhibit that the original planar wave becomes bent when the incident wave gradually approaches the dielectric cylinder. The resulting scattered wave is perfectly absorbed as it enters into the absorbing layer. For the validation sake, the currently predicted results are compared with the analytical result at different values of ϵ_r. As Figs. 13 and

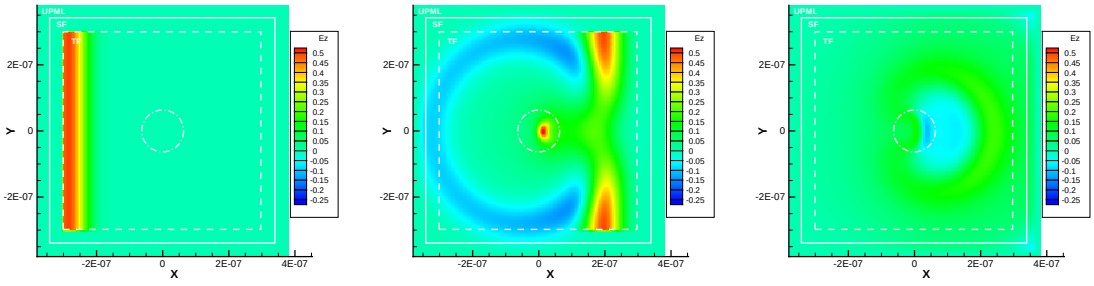

(a) (b) (c)

Figure 12: The predicted contour plots of E_z in TF/SF containing a cylinder scatter. (a) time step$=600$; (b) time step$=1200$; (c) time step$=1600$.

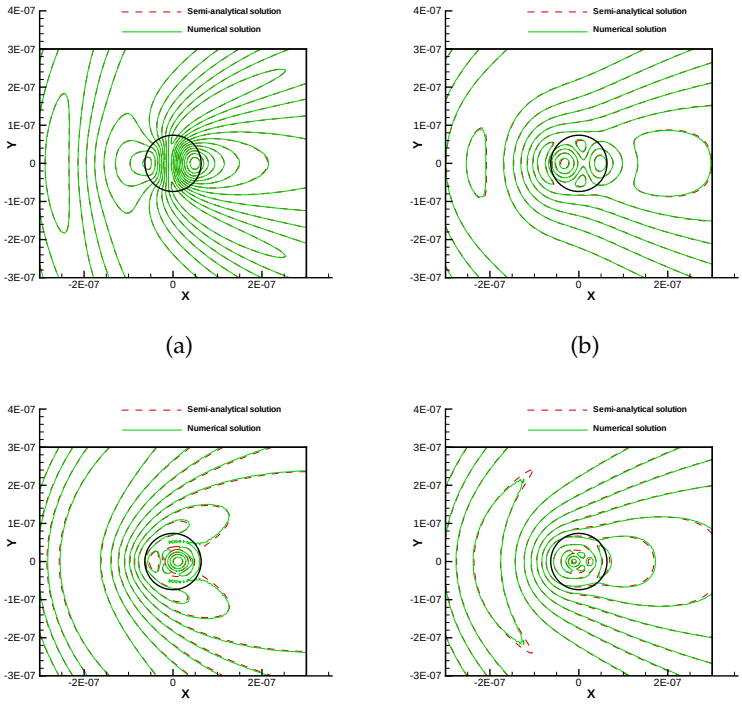

(a) (b)

(c) (d)

Figure 13: Comparison of the four predicted contour values of E_z. (a) $\varepsilon_r = 12$; (b) $\varepsilon_r = 20$; (c) $\varepsilon_r = 50$; (d) $\varepsilon_r = 100$.

14 show, the observed excellent agreement with the exact solution confirms the proper scheme development for the Maxwell's equations solved in the total/scatter and the modified Maxwell's equations used in the absorbing layer.

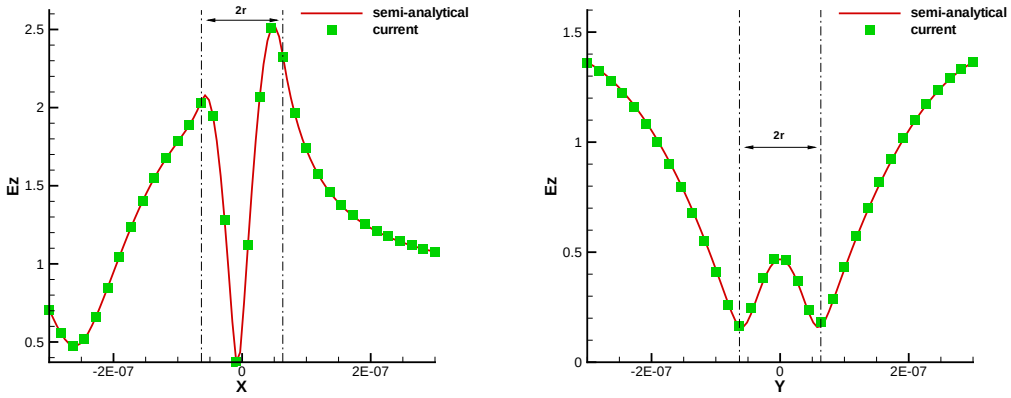

(a) (b)

Figure 14: Comparison of the E_z profiles for the case investigated at $\epsilon_r = 12$. (a) $E_z(x,0)$; (b) $E_z(0,y)$.

7.2 Photonic crystal L-shaped bent waveguide problem

A platform containing many photonic crystals (PC) is promising to get an integrated optoelectronic circuits. The popularity of employing photonic crystals is due to their displayed band gaps that allow them to be able to effectively affect the light propagation. In this study we consider a two-dimensional lattice of infinite vertical rods (dielectric pillars) in the $x-y$ plane. The dielectric constant (or relative permittivity) of the medium surrounding the uniformly distributed pillars is set at the value of 1, while the dielectric constant for the pillars is assumed to be $\epsilon_r = 11.56$. As schematic in Fig. 15(a), the waveguide of width $\frac{w}{a} = 2$ is generated by removing one vertical and one row of the pillars, leading to a L-shaped defect channel. A light whose frequency belonging to the photonic band gap is confined in the defect channel. The transverse magnetic mode is incident on the array and propagates from left to right. For getting a wider range of the photonic band gap, the radius of these pillars is chosen as $0.2a$, where the lattice constant a $(=515\ nm)$ denotes the length between the centroids of two adjacent pillars.

The PC-based L-shaped bent waveguide problem is simulated at $\Delta t = 0.026685\ fs$ and $\Delta x = \Delta y = 40\ nm$. The perfectly matched layer attached to the scatter field can indeed absorb the wave. Otherwise, unphysical wave will re-enter to the domain of interest and it will in turn interact with the propagation wave, leading to an erroneous wave scattering in the lattices. Fig. 15 shows the time-evolving contours of E_z computed at the normalized frequency $= 0.353$ $(\frac{c}{a})$ (or wavelength = 1458.92 nm), where c denotes the speed of light. In Fig. 16, the time-varying energy density in the investigated lattice is also plotted at the same resonant frequency. We can clearly see that the optical wave proceeds efficiently through the 90°-bend and the electric field is concentrated mostly in the L-shaped defect channel. Comparison of the current result with the result of Mekis et

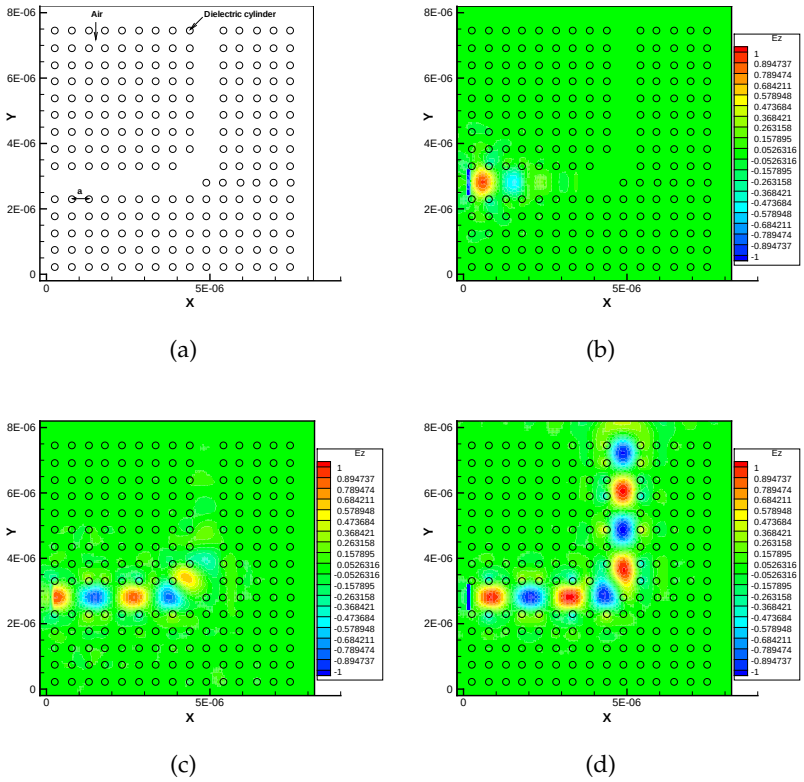

Figure 15: Snapshot of the computed time evolving E_z contours in the PC-based L-shape waveguide schematic in (a) at the normalized frequency 0.353(c/a). (b) time step$=740$; (c) time step$=1800$; (d) time step$=5670$.

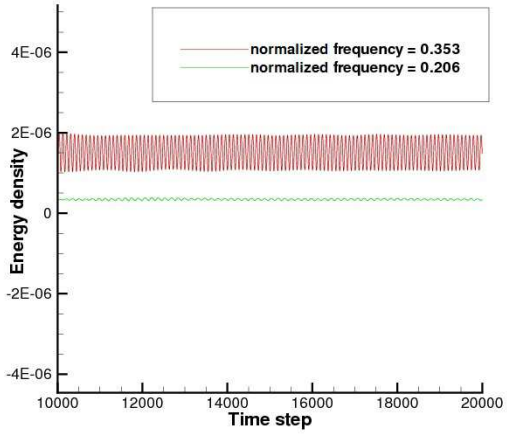

Figure 16: Comparison of the computed time-varying values of the energy density defined in (10) for the L-shape PC investigated at two different normalized frequencies.

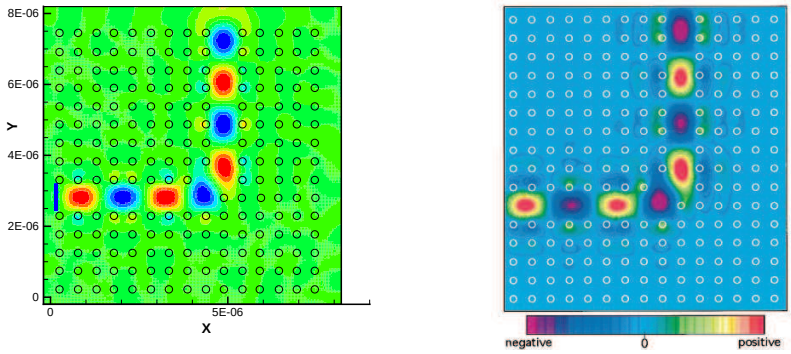

(a) (b)

Figure 17: Snapshot of the computed E_z field values at the time step 5670 in the PC-based L-shape waveguide at the normalized frequency 0.353(c/a). (a) Present method; (b) Mekis et al. [32].

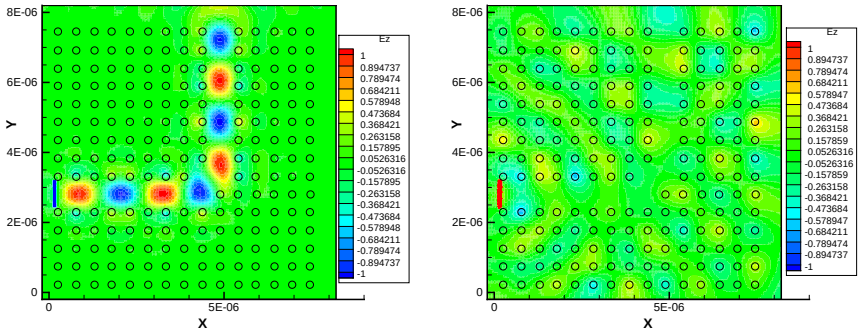

(a) (b)

Figure 18: Comparison of the computed E_z field values at two normalized frequencies in the PC-based L-shape waveguide at the time step 5670. (a) 0.353(c/a); (b) 0.206(c/a).

al. [32] is illustrated in Fig. 17. The cases with two incident wave frequencies, which are 0.353 $(\frac{c}{a})$ and 0.206 $(\frac{c}{a})$, are investigated as well and the simulated results are plotted in Fig. 18.

8 Conclusions

To develop a good discretization scheme, both of the symplecticity and conservation properties embedded in the Maxwell's equations should be numerically retained all the time. This guideline prompts us to employ the explicit partitioned Runge-Kutta symplectic time integrator to preserve Hamiltonian structure in the Maxwell's equations. We also develop the space-centered scheme which has the smallest difference between the numerical dispersion relation equation and its exact counterpart. The temporally second-order

accurate Maxwell's solutions are also shown to computationally satisfy the Gauss' law for the magnetism and electricity. In the current non-staggered grid approach, the electric and magnetic field solutions computed from the Faraday's and Ampère's equations have been properly corrected to compensate for the omission of Gauss's law. Several analytic and benchmark problems have been solved and the predicted solutions are shown to have the excellent agreement with the exact and the referenced numerical solutions.

Acknowledgments

This work was supported by the National Science Council of the Republic of China under the Grants NSC96-2221-E-002-293-MY2, NSC96-2221-E-002-004, and CQSE97R0066-69.

References

[1] J. X. Cai, Y. S. Wang, B. Wang, and B. Jiang, New multisymplectic self-adjoint scheme and its composition scheme for the time-domain Maxwell's equations, Journal of Mathematical Physics, 47 (2006), pp. 1-18.
[2] K. S. Yee, Numerical solution of initial boundary value problems involving Maxwell's equations in isotropic media, IEEE Transactions on Antenna Propagation, AP4 (1966), pp. 302-307.
[3] C.-D. Munz, P. Ommes, R. Schneider, E. Sonnendrücker, and U. Voβ, Divergence correction techinques for Maxwell solvers based on a hyperbolic model, Journal of Computational Physics, 161 (2000), pp. 484-511.
[4] B. Cockburn, F. Li, and C.-W. Shu, Locally divergence-free discontinuous Galerkin methods for the Maxwell equations, Journal of Computational Physics, 194 (2004), pp. 588-610.
[5] T. J. Bridges and S. Reich, Multi-symplectic integration numerical scheme for Hamiltonian PDEs that conserves symplecticity, Phys. Lett. A, 284 (2001), pp. 184-193.
[6] M. Born and E. Wolf, Principles of Optics, Pergamon Press, Oxford, (1964).
[7] L. H. Kong, J. L. Hong, and J. J. Zhang, Splitting multisymplectic integrators for Maxwell's equations, Journal of Computational Physics, 229 (2010), pp. 4259-4278.
[8] N. Anderson and A. M. Arthurs, Helicity and variational principles for Maxwell's equations, Int. J. Electron, 54 (1983), pp. 861-864.
[9] J. U. Brackbill and D. C. Barnes, The effect of nonzero product of magnetic gradient and B on the numerical solution of the magnetohydrodynamic equations, Journal of Computational Physics, 35 (1980), pp. 426-430.
[10] L. D. Landau, E. M. Lifshitz and L. P. Pitaevskii, Electrodynamics of Continuous Media, Pergamon Press, Oxford, (1984).
[11] B. Jiang, J. Wu, and L. A. Povinelli, The origin of spurious solutions in computational electromagnetics, NASA-TM-10692, E-9633, ICOMP-95-8, 1995.
[12] F. Assous, P. Degond, E. Heintze, P. A. Raviart, and J. Serger, On a finite-element method for solving the three-dimensional Maxwell equations, Journal of Computational Physics, 109 (1993), pp. 222-237.
[13] T. W. H. Sheu, Y. W. Hung, M. H. Tsai, and J. H. Li, On the development of a triple-preserving Maxwell's equations solver in non-staggered grids, Int. J. Numer. Meth. in Fluids, 63 (2010), pp. 1328-1346.

[14] C. Greif, D. Li, D. Schötzau, and X. Wei, A mixed finite element method with exactly divergence-free velocities for incompressible magnetohydrodynamics, Computer Methods in Applied Mechanics and Engineering, 199 (2010), pp. 2840-2855.
[15] P. Pinho, M. O. Domingues, P. J. S. G. Ferrira, S. M. Gomes, A. Gomide, J. R. Pereira, Interpolating wavelets and adaptive finite difference schemes for solving Maxwell's equations: The effects of gridding, IEEE Trans. on Magnetics, 43 (3) (2007), pp. 1013-1022.
[16] Y. Liu, Fourier analysis of numerical algorithms for the Maxwell equations, J. Computational Physics, 124, (1996), pp. 396-416.
[17] C.-D. Munz, P. Ommes, R. Schneider, A three-dimensional finite-volume solver for the Maxwell equations with divergence cleaning on unstructured meshes, Computer Physics Communications, 130, (2000), pp. 83-117.
[18] J. M. Sanz-Serna, Symplectic Runge-Kutta and related methods: recent results, Physica D, (1992), pp. 293-302.
[19] T. H. Monovasills, Z. Kalogiratou, and T. E. Simos, Symplectic partitioned Runge-Kutta methods with minimal phase-lag, Computer Physics Communications, 181 (2010), pp. 1251-1254.
[20] L. L. Jiang, J. F. Mao, and X. L. Wu, Symplectic finite-difference time-domain method for Maxwell equations, IEEE Transactions on Magnetics, 42(8) (2006), pp. 1991-1995.
[21] A. Taflove and K. R. Umashankar, The finite-difference time-domain method for numerical modeling of electromagnetic wave interactions, Electromag., 10(1) (1990), pp. 105-126.
[22] S. Wang and F. L. Teixeira, Dispersion relation-preserving FDTD algorithms for large-scale three-dimensional problems, IEEE Transactions on Antennas and Propagation, 51(8) (2003), pp. 1818-1828.
[23] J. K. Kim and D. J. Lee, Optimized compact finite difference schemes with maximun resolution, AIAA J., 34(5) (1996), pp. 887-893.
[24] C. K. W. Tam and J. C. Webb, Dispersion-relation-preserving finite difference schemes for computational acoustics, Journal of Computational Physics, 107 (1993), pp. 262-281.
[25] S. K. Lele, Compact finite difference schemes with spectral-like resolution, Journal of Computational Physics, 103 (1992), pp. 16-42.
[26] C. Bogry and C. Bailly, A family of low dispersive and low dissipative explicit schemes for flow and noise computations, Journal of Computational Physics, 194 (2004), pp. 194-214.
[27] L. Gao, B. Zhang, and D. Liang, The splitting finite-difference time-domain methods for Maxwell's equations in two dimensions, J. Comput. Applied Math., 205 (2007), pp. 207-230.
[28] Z. S. Sacks, D. M. Kinsland, R. Lee, and J. F. Lee, A perfectly matched anisotropic absorber for use as an absorbing boundary condition, IEEE T. Antenn. Propag., 43 (1995), pp. 1640-1643.
[29] S. D. Gedney, An anisotropic perfectly matched layer absorbing media for the truncation of FDTD lattices, IEEE T. Antenn. Propag., 44 (1996), pp. 1630-1639.
[30] M. Born and E. Wolf, Principles of Optics, Cambridge University Press, Cambridge, (1999) pp.759-774.
[31] J. P. Berenger, A perfectly matched layer for the absorption of electromagnetic waves, Journal of Computational Physics, 114 (1994), pp. 185-200.
[32] A. Mekis, J. C. Chen, I. Kurland, S. Fan, P. R. Villeneuve, and J. D. Joannopoulos, High transmission through sharp bends in photonic crystal waveguides, Physical Review Letters, 77 (1996), pp. 3787-3790.